Mechanism for Southward Shift of Zonal Wind Anomalies during the Mature Phase of ENSO

YUHAN GONG[a] AND TIM LI[a,b]

[a] *Key Laboratory of Meteorological Disaster, Ministry of Education (KLME), Joint International Research Laboratory of Climate and Environmental Change (ILCEC), Collaborative Innovation Center on Forecast and Evaluation of Meteorological Disasters (CIC-FEMD), Nanjing University of Information Science and Technology, Nanjing, China*

[b] *International Pacific Research Center and Department of Atmospheric Sciences, School of Ocean and Earth Science and Technology, University of Hawai'i at Mānoa, Honolulu, Hawaii*

(Manuscript received 26 January 2021, in final form 26 July 2021)

ABSTRACT: The cause of the southward shift of anomalous zonal wind in the central equatorial Pacific (CEP) during ENSO mature winter was investigated through observational analyses and numerical model experiments. Based on an antisymmetric zonal momentum budget diagnosis using daily ERA-Interim data, a two-step physical mechanism is proposed. The first step involves advection of the zonal wind anomaly by the climatological mean meridional wind. The second step involves the development of an antisymmetric mode in the CEP, which promotes a positive contribution to the observed zonal wind tendency by the pressure gradient and Coriolis forces. Two positive feedbacks are responsible for the growth of the antisymmetric mode. The first involves the moisture–convection–circulation feedback, and the second involves the wind–evaporation–SST feedback. General circulation model experiments further demonstrated that the boreal winter background state is critical in generating the southward shift, and a northward shift of the zonal wind anomaly is found when the same SST anomaly is specified in boreal summer background state.

KEYWORDS: Wind; ENSO; Interannual variability

1. Introduction

El Niño–Southern Oscillation (ENSO) is the dominant interannual mode in the tropics with a large fluctuation in sea surface temperature anomalies (SSTA), zonal wind, and sea level pressure in the tropical Pacific basin swinging between a warm (El Niño) and a cold (La Niña) phase on a 2–7-yr period (Rasmusson and Carpenter 1982; Cane and Zebiak 1985; Philander 1990; Li 1997a; Wallace et al. 1998). Although the main atmospheric convective activity associated with ENSO is confined in the tropics, it can exert a remote impact on global climate (Ropelewski and Halpert 1987; Trenberth and Caron 2000; Li and Hsu 2018; Taschetto et al. 2020). Because of its great climate impact, understanding and predicting ENSO has attracted a great attention in the climate research community and ENSO dynamics have been widely explored since the ENSO concept was proposed in early 1980s.

An important feature of ENSO evolution is seasonal phase locking to annual cycle. A typical ENSO event starts to develop in boreal spring and reaches a peak in boreal winter, with a maximum SSTA tendency in boreal autumn (Li 1997a). Factors that affect the ENSO phase locking were investigated previously (e.g., Li 1997a; Wang et al. 2000; An and Wang 2001; Dommenget and Yu 2016; Wengel et al. 2018; Bayr et al. 2021). The first possible mechanism is a season-dependent coupled instability, due to the fact that maximum mean upwelling and maximum zonal SST gradient along the equatorial Pacific appear in autumn so that both the Bjerknes thermocline feedback and zonal advective feedback are strongest in the season (Li 1997a; Li and Hsu 2018). The second mechanism is associated with the Philippine Sea anomalous anticyclone because anomalous easterly winds in the western equatorial Pacific associated with the anticyclone trigger upwelling oceanic Kelvin waves to terminate ENSO events (Wang et al. 2000; An and Wang 2001). Additional processes relevant to the phase locking are the seasonality of the shortwave/cloud cover feedback (Dommenget and Yu 2016) and seasonality of the latent heat flux feedback and mixed layer depth (Bayr et al. 2021). Through quantitative calculations, the role of seasonal variation of ENSO dynamic and thermodynamic feedbacks related to the annual cycle on the ENSO phase locking was revealed (Stein et al. 2010; Wengel et al. 2018; Bayr et al. 2021). Some research argued that the southward shifting of the zonal wind anomalies in ENSO mature phase is helpful to terminate ENSO events (Harrison and Vecchi 1999; Vecchi and Harrison 2003; Spencer 2004; Lengaigne et al. 2006; Lengaigne and Vecchi 2010; McGregor et al. 2012; McGregor et al. 2013; Abellán and McGregor 2016). Abellán et al. (2017) noted that CMIP5 models that captured the zonal wind shift could simulate the phase locking of ENSO more realistically.

The focus of this article is the interesting feature that is the meridional shift of the maximum zonal wind anomaly during the life cycle of ENSO (Harrison 1987; Harrison and Vecchi 1999). When El Niño occurs with positive SSTA, a maximum

Supplemental information related to this paper is available at the Journals Online website: https://doi.org/10.1175/10.1175/JCLI-D-21-0078.s1.

Corresponding author: Tim Li, timli@hawaii.edu

DOI: 10.1175/JCLI-D-21-0078.1

low-level westerly anomaly and a positive precipitation anomaly appear in the central equatorial Pacific (CEP). During the ENSO developing phase, the zonal wind anomaly field in CEP is approximately symmetric about the equator, with a maximum at the equator. The maximum zonal wind anomaly then shifts southward during the mature phase of ENSO (DJF). After that, it gradually goes back toward the equator. The shift of the maximum zonal wind anomaly might weaken the equatorial thermocline response, altering the ENSO recharge/discharge process (McGregor et al. 2012, 2013). While the maximum zonal wind shifts southward during the ENSO mature phase, the maximum SSTA center stays approximately on the equator. This poses a science question as to what causes an equatorially asymmetric wind response to a symmetric SSTA forcing. A possible factor is the background SST annual cycle (Spencer 2004; Lengaigne et al. 2006; Vecchi 2006). In boreal winter, the maximum climatological SST appears south of the equator due to the solar radiative forcing. As tropical convection can only be triggered above a certain SST threshold (Gadgil et al. 1984; Graham and Barnett 1987), the SSTA south of equator, superposed on the higher climatological mean SST, may trigger local anomalous convection more easily. Through a simple model simulation, McGregor et al. (2012) found that a weakening of climatological wind speed associated with the seasonal cycle of the South Pacific convergence zone (SPCZ) might be responsible for the southward wind shift through its modulation of the Ekman pumping coefficient. Such a result, however, requires further validation from the observational analysis and general circulation model simulations. Based on the pattern of the second EOF mode of the tropical Pacific surface wind anomalies, Stuecker et al. (2013, 2015) argued that the southward shift of the zonal wind anomaly resulted from a nonlinear interaction between ENSO and the annual cycle, which generated a near annual period combination mode.

In this study, we intend to re-examine this outstanding ENSO dynamics problem through a combined observational diagnosis and GCM modeling approach. A new diagnosis method is put forward to quantitatively investigate the physical mechanism responsible for the southward shift of the zonal wind anomaly during ENSO mature phase. Each variable is separated into a symmetric and an antisymmetric component. By diagnosing the antisymmetric component of the zonal momentum budget, we aim to reveal specific processes that give rise to the asymmetric zonal wind tendency. A full-physics GCM is further employed to validate the diagnosis result. The remaining part of this paper is organized as follows. Section 2 introduces data and methods used in this study. Section 3 illustrates the observed evolution characteristics of the asymmetric wind pattern. In section 4 the zonal momentum budget is diagnosed to explore the specific physical processes responsible for the southward wind shift. A set of sensitivity GCM experiments are further carried out to verify the diagnosis result above in section 5. Finally, conclusions and discussion are given in section 6.

2. Data and methods

a. Data

The monthly SST field used in this study is from the Hadley Centre Sea Ice and Sea Surface Temperature dataset (HadISST; Rayner et al. 2003) with 1° × 1° horizontal resolution. Daily atmospheric fields including three-dimensional wind (u, v, ω) and monthly variables including specific humidity, geopotential height, and precipitation are from the European Centre for Medium-Range Weather Forecasts (ECMWF) interim reanalysis (ERA-Interim; Dee and Uppala 2009) with 0.5° × 0.5° resolution. The current analysis covers the period from 1979 to 2018.

b. Methods

To investigate the contrast between the Southern Hemisphere (SH) and Northern Hemisphere (NH), all variables are decomposed into a symmetric and an antisymmetric component relative to the equator, following Li (1997b). The symmetric and antisymmetric components are calculated based on the following formulas:

$$\mathrm{var}_s(y) = \frac{\mathrm{var}(y) + \mathrm{var}(-y)}{2}, \tag{1}$$

$$\mathrm{var}_a(y) = \frac{\mathrm{var}(y) - \mathrm{var}(-y)}{2}, \tag{2}$$

where y denotes latitude, and subscripts s and a represent the symmetric and antisymmetric component of a variable except for the meridional wind field. For the meridional wind field, its equatorially symmetric and antisymmetric components are defined as follows:

$$v_s(y) = \frac{v(y) - v(-y)}{2}, \tag{3}$$

$$v_a(y) = \frac{v(y) + v(-y)}{2}. \tag{4}$$

To investigate specific physical processes that cause the equatorial asymmetry of the zonal wind anomaly, an antisymmetric zonal wind tendency equation is diagnosed. The antisymmetric zonal momentum budget equation can be written as follows:

$$\left(\frac{\partial u}{\partial t}\right)'_a = -\left(u\frac{\partial u}{\partial x}\right)'_a - \left(v\frac{\partial u}{\partial y}\right)'_a - \left(\omega\frac{\partial u}{\partial p}\right)'_a + fv'_a - \left(\frac{\partial \varphi}{\partial x}\right)'_a + (F_x)'_a, \tag{5}$$

where a prime denotes the interannual anomaly; subscript a denotes the antisymmetric component of each term; u, v, and ω denote the three-dimensional (3D) wind, $\partial u/\partial t$ denotes the zonal wind tendency, $-u(\partial u/\partial x)$, $-v(\partial u/\partial y)$, and $-\omega(\partial u/\partial p)$ are the 3D advection term, f is the Coriolis parameter, φ denotes the geopotential height, and F_x denotes the apparent momentum sink term that consists of turbulence viscosity and surface friction. Following the concepts of apparent heat source and moisture sink (Yanai et al. 1973), we calculated this apparent momentum sink term F_x based on the original zonal momentum equation using daily reanalysis raw data. All terms on the left- and right-hand sides of the original momentum equation except F_x could be calculated first. Then F_x can be determined based on these terms. To ensure

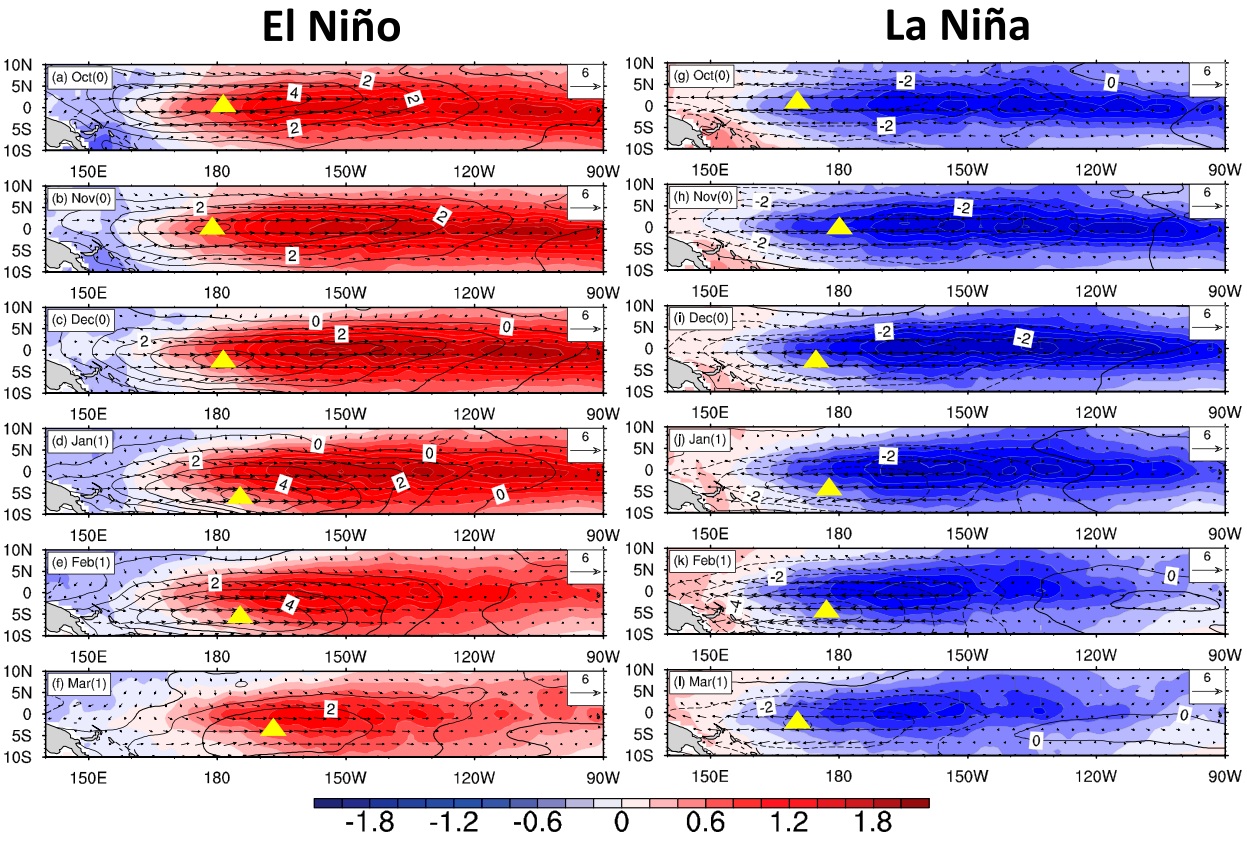

FIG. 1. Composite monthly evolutions of the SST (shading; °C), 850-hPa wind (vector; m s^{-1}) and 850-hPa zonal wind [contour; interval: 1 m s^{-1}; solid (dashed) line indicates westerly (easterly)] anomaly fields from Oct(0) to Mar(1) during (a)–(f) El Niño and (g)–(l) La Niña; the 0 and 1 in parentheses after month names denote an ENSO developing and decaying year respectively. The triangles mark the maximum center of zonal wind anomalies.

the robustness of the budget analysis result, a parallel diagnosis using JRA-55 reanalysis data is also conducted. The resulting momentum budget is consistent with that derived from the ERA-Interim data. Below only the analysis from ERA-Interim is shown.

3. Observed structure and evolution characteristics of the zonal wind anomaly during ENSO

To obtain the composite zonal wind pattern and evolution features, we select the following El Niño (1982/83, 1986/87, 1987/88, 1991/92, 1994/95, 1997/98, 2002/03, 2004/05, 2006/07, 2009/10, and 2015/16) and La Niña (1983/84, 1984/85, 1988/89, 1995/96, 1996/97, 1998/99, 1999/2000, 2005/06, 2007/08, 2008/09, 2010/11, 2011/12, and 2016/17) cases for a composite analysis. Following Chen et al. (2016), El Niño (La Niña) cases are selected as the SST anomaly averaged over the Niño-3.4 region in boreal winter exceeds one positive (negative) standard deviation. The composite evolutions of SST and 850-hPa wind anomalies for El Niño and La Niña are shown in Fig. 1. For El Niño (La Niña), pronounced westerly (easterly) anomalies occur in the CEP. There is a slight difference in the zonal location of the zonal wind anomaly between the El Niño and La Niña composites. The easterly anomalies during La Niña are located farther toward the west compared to the westerly anomalies during El Niño, which is somehow related to the zonal asymmetry of SSTA pattern (Kang and Kug 2002) and rising branch of the Walker circulation (Bayr et al. 2014, 2018) between El Niño and La Niña.

In Oct(0) and Nov(0) [that is, October and November in an ENSO developing year, denoted by (0); an ENSO decaying year is denoted by (1)], the maximum center of the zonal wind anomaly is located approximately on the equator. In Dec(0), as the intensity of both the anomalous SST and wind reaches a maximum, the center of the zonal wind anomaly starts to move southward. In Jan(1) and Feb(1), the maximum center of the zonal wind anomaly can reach as far as 8°S.

Figure 1 illustrates that the zonal range of the main southward shift of the zonal wind anomaly appears at 160°E–150°W and the time period for such a shift happens in D(0)JF(1). To further illustrate the vertical structure of the zonal wind shift, Fig. 2 shows the meridional–vertical distributions of the zonal wind anomaly field averaged over 160°E–150°W from SON(0) to MAM(1) for both El Niño and La Niña composites. It is seen

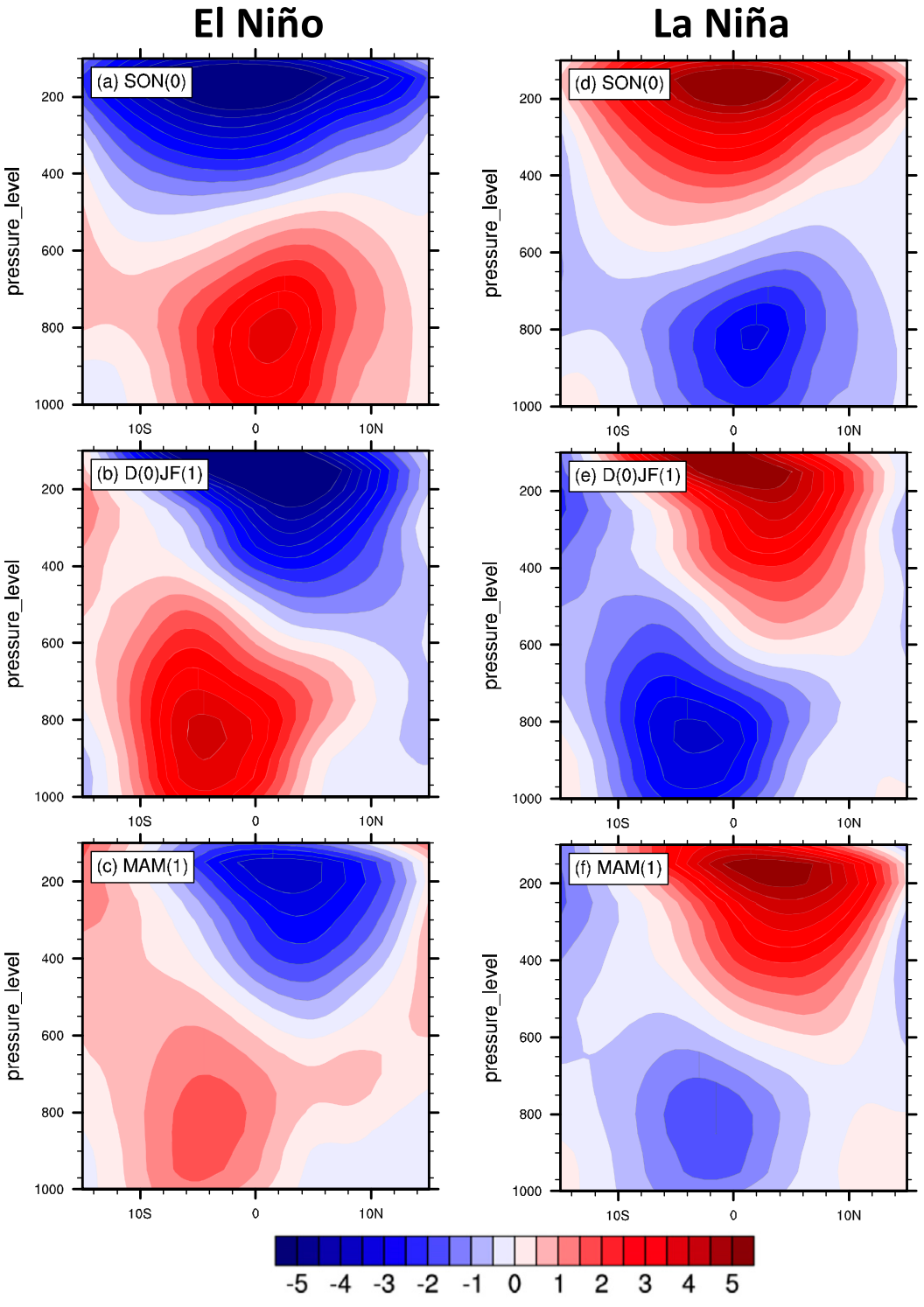

FIG. 2. The meridional–vertical cross section along 160°E–150°W of composite zonal wind anomalies u' (m s^{-1}) from SON(0) to MAM(1) during (a)–(c) El Niño and (d)–(f) La Niña.

that during boreal autumn [SON(0)], the anomalous zonal wind for both El Niño and La Niña is approximately symmetric relative to the equator. In D(0)JF(1) as ENSO reaches its peak phase, the maximum zonal wind center moves southward. The southward shift of the zonal wind anomaly is confined in the lower troposphere (1000–700 hPa). Thus, next we will focus on diagnosing the zonal momentum budget terms averaged over 1000–700 hPa.

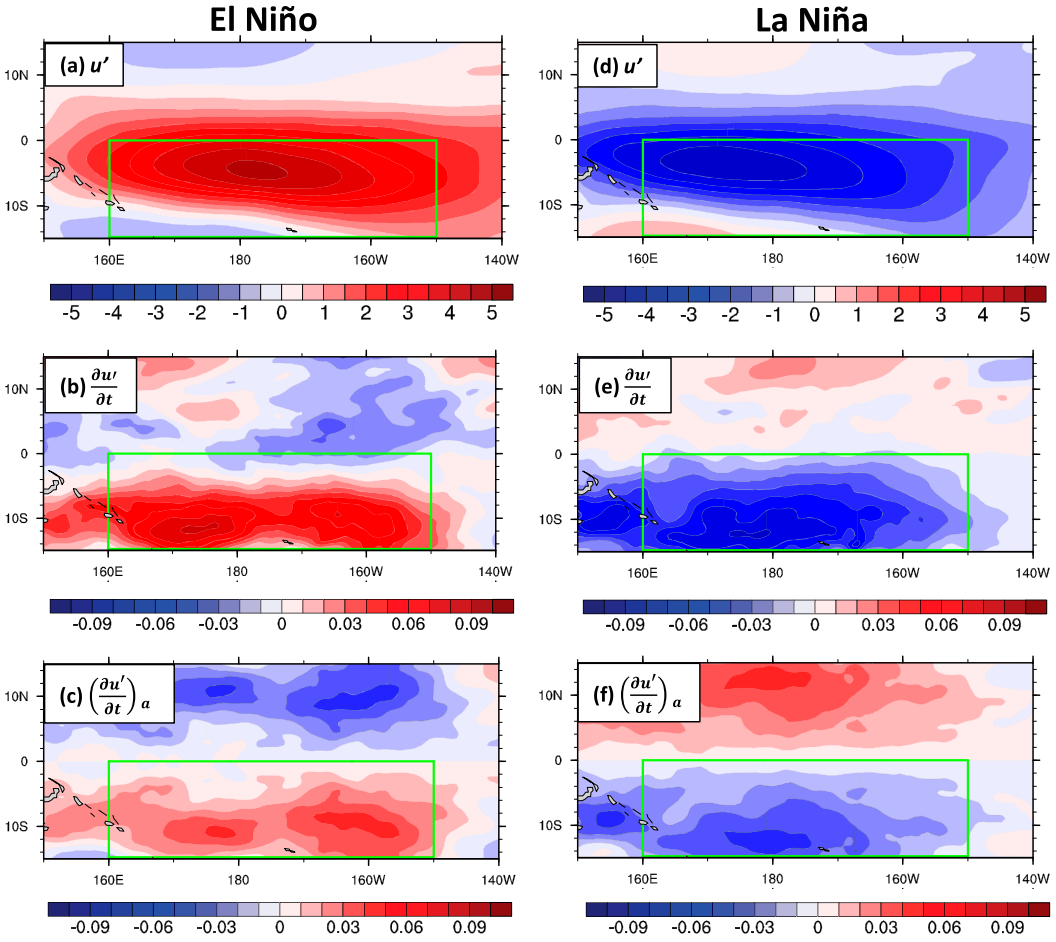

FIG. 3. Composite patterns of anomalous zonal wind u' (m s^{-1}), zonal wind tendency $\partial u'/\partial t$ (10^{-5} m s^{-2}), and the antisymmetric component of the zonal wind tendency averaged over 1000–700 hPa in D(0)JF(1) for (left) El Niño and (right) La Niña. The green box denotes the key diagnosis region (160°E–150°W, 0°–15°S) for the zonal momentum budget.

4. Antisymmetric zonal momentum budget diagnosis

To investigate the specific physical processes that cause the zonal wind shift, we diagnosed the antisymmetric zonal momentum budget. The reason to focus on the antisymmetric momentum budget is to reveal key processes that cause the equatorial asymmetry. For the reader's convenience, the full budget that includes the combined antisymmetric and symmetric components is shown in Figs. S1 and S2 in the online supplemental material. The top panels of Fig. 3 show the anomalous zonal wind and zonal wind tendency fields for both the El Niño and La Niña composites in D(0)JF(1). Note that as the maximum zonal wind anomaly shifts south of the equator (Figs. 3a,d), there is an obvious asymmetry relative the equator in the zonal wind tendency field; that is, there is in general a positive (negative) zonal wind tendency south (north) of the equator for El Niño, while it is opposite for La Niña (Figs. 3b,e).

The lower panel of Fig. 3 displays the antisymmetric component of the zonal wind tendency field (Figs. 3c,f). To the first order of approximation, the patterns in the lower panels resemble the middle panel. Such a contract of the zonal wind tendency between SH and NH is strongest in boreal winter compared to other seasons. In the following we will pay primary attention to the generation of the maximum antisymmetric zonal momentum tendency over 0°–15°S, 160°E–150°W (i.e., green box in Fig. 3).

Because of its nearly mirror image of the zonal wind tendency patterns between El Niño and La Niña (figures not shown), hereafter we will focus on the antisymmetric zonal momentum budget diagnosis averaged over 1000–700 hPa for El Niño. The horizontal patterns of each budget term on the right-hand side of Eq. (5) are shown in Fig. 4. Note that the antisymmetric meridional advection term $\{-[v(\partial u/\partial y)]'_a\}$, the Coriolis force term (fv'_a), and the pressure gradient force term $[-(\partial\varphi/\partial x)'_a]$ all contribute positively to the increase of the anomalous westerly in the SH (Figs. 4b,d,e), while the apparent momentum sink term $[(F_x)'_a]$ tends to damp the westerly tendency (Fig. 4f). The antisymmetric zonal advection term $\{-[u(\partial u/\partial x)]'_a\}$ and vertical advection term $\{-[\omega(\partial u/\partial p)]'_a\}$ have little effect.

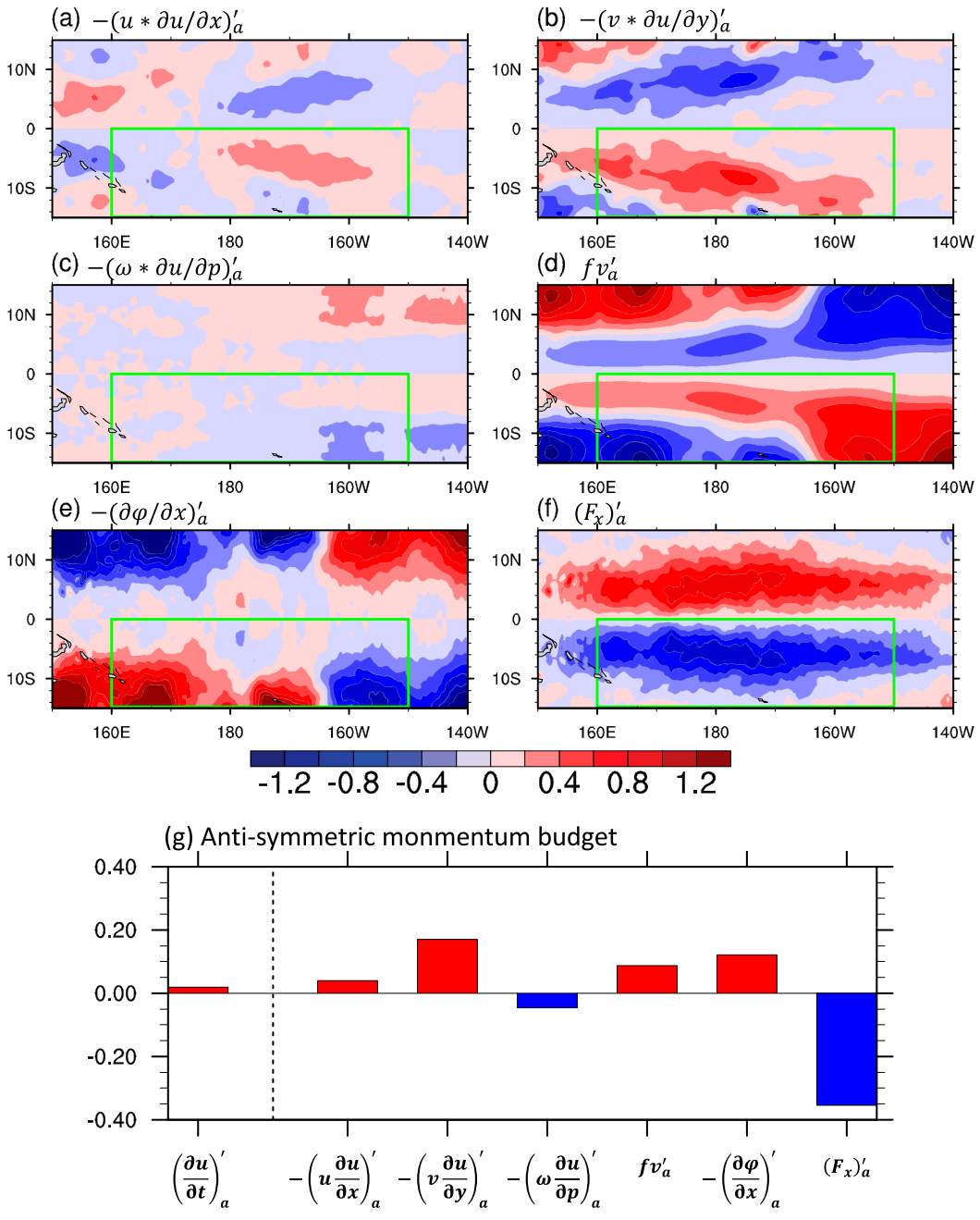

FIG. 4. The composite antisymmetric zonal momentum budget results in D(0)JF(1) for El Niño: (a) $-[u(\partial u/\partial x)]'_a$, (b) $-[v(\partial u/\partial y)]'_a$, (c) $-[\omega(\partial u/\partial p)]'_a$, (d) fv'_a, (e) $-(\partial\varphi/\partial x)'_a$, and (f) $(F_x)'_a$ (10^{-5} m s^{-2}). The green box is 160°E–150°W, 0°–15°S. (g) The averaged results over the green boxes of (a)–(f).

The relative contributions of the momentum budget terms on the right-hand side of Eq. (5) to the zonal wind tendency are estimated based on the average values over the green box region (0°–15°S, 160°E–150°W), and the result is shown in Fig. 4g. The left bar in Fig. 4g shows the antisymmetric zonal wind tendency, which is balanced by summation of six bars to its right. The largest contribution to the zonal wind tendency arises from the antisymmetric meridional advection term $-[v(\partial u/\partial y)]'_a$, followed by the pressure gradient force term $-(\partial\varphi/\partial x)'_a$ and the Coriolis force term fv'_a. In the following we will investigate physical mechanisms associated with each of these terms.

a. Meridional advection term

By further decomposing each variable into a climatological mean state component and an interannual anomaly component,

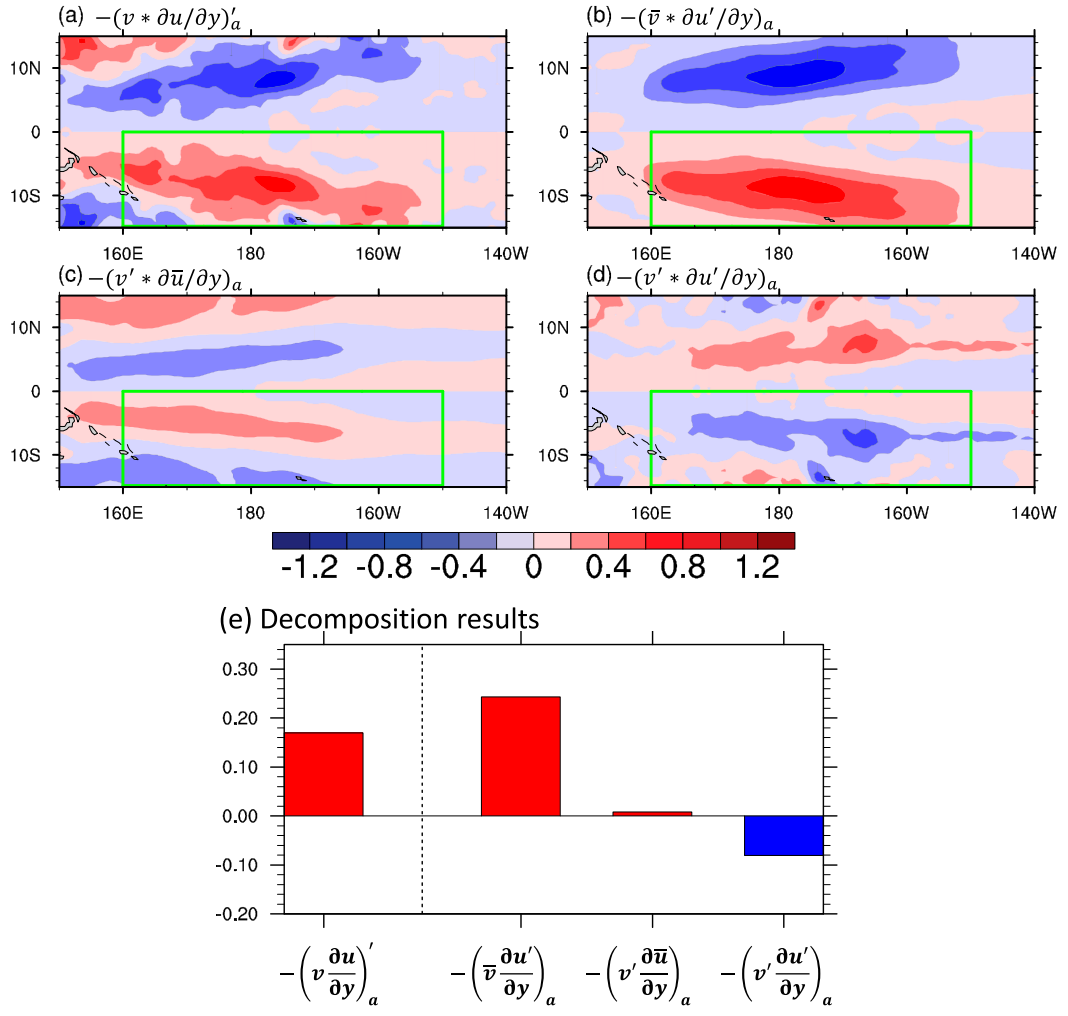

FIG. 5. Horizontal distributions of (a) $-[v(\partial u/\partial y)]'_a$, (b) $-[\overline{v}(\partial u'/\partial y)]_a$, (c) $-[v'(\partial \overline{u}/\partial y)]_a$, and (d) $-[v'(\partial u'/\partial y)]_a$ in D(0)JF(1) for El Niño (10^{-5} m s^{-2}). (e) The averaged results of (a)–(d) over the green box.

the antisymmetric meridional advection term $-[v(\partial u/\partial y)]'_a$ can be written as

$$-\left(v\frac{\partial u}{\partial y}\right)'_a = -\left(\overline{v}\frac{\partial u'}{\partial y}\right)_a - \left(v'\frac{\partial \overline{u}}{\partial y}\right)_a - \left(v'\frac{\partial u'}{\partial y}\right)_a, \qquad (6)$$

where a bar denotes the climatological mean state component and a prime denotes the interannual anomaly component. The three terms in the right-hand side of Eq. (6) represent 1) the advection of the anomalous zonal wind u' by the mean meridional wind $\overline{v}$, 2) the advection of the mean zonal wind $\overline{u}$ by anomalous meridional wind v', and 3) the nonlinear term denoting the advection of the anomalous zonal wind by the anomalous meridional wind.

Figure 5 shows the decomposition result. It is obvious that the antisymmetric meridional advection term is primarily attributed to the advection of the anomalous zonal wind by the mean meridional wind. To quantitatively compare the relative roles of these advective terms, we calculated the average values of the four terms over the key analysis box (0°–15°S, 160°E–150°W) (Fig. 5e). It is clear that the antisymmetric advection of the anomalous zonal wind u' by the mean meridional wind $\overline{v}$ [i.e., $-[\overline{v}(\partial u'/\partial y)]_a$] is the dominant term. The term $-[v'(\partial \overline{u}/\partial y)]_a$ has little effect, while the term $-[v'(\partial u'/\partial y)]_a$ has even a negative impact.

Through the following decomposition,

$$-\overline{v}\frac{\partial u'}{\partial y} = -(\overline{v}_s + \overline{v}_a)\frac{\partial (u'_s + u'_a)}{\partial y}$$
$$= -\overline{v}_s\frac{\partial u'_s}{\partial y} - \overline{v}_a\frac{\partial u'_s}{\partial y} - \overline{v}_s\frac{\partial u'_a}{\partial y} - \overline{v}_a\frac{\partial u'_a}{\partial y}, \qquad (7)$$

the antisymmetric component of the anomalous zonal wind advection by the mean meridional wind can be written as

$$-\left(\overline{v}\frac{\partial u'}{\partial y}\right)_a = -\overline{v}_a\frac{\partial u'_s}{\partial y} - \overline{v}_s\frac{\partial u'_a}{\partial y}. \qquad (8)$$

The top panels of Fig. 6 show the horizontal patterns of two terms on the right-hand side of Eq. (8). It is seen that the

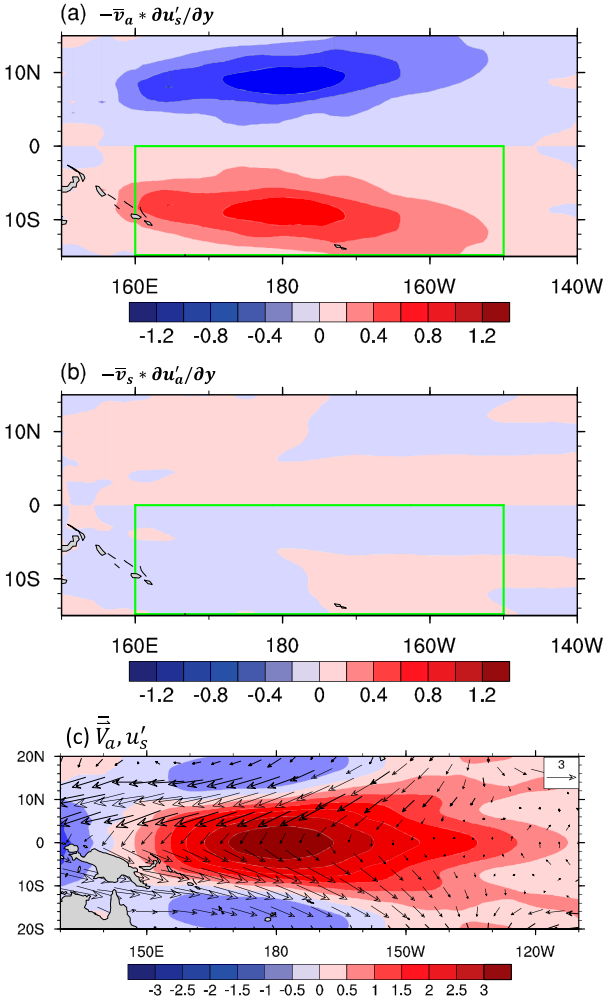

FIG. 6. Horizontal distributions of (a) $-\overline{v}_a(\partial u'_s/\partial y)$ and (b) $-\overline{v}_s(\partial u'_a/\partial y)$ in D(0)JF(1) for El Niño (10^{-5} m s^{-2}). (c) Climatic antisymmetric wind in DJF (vector; m s^{-1}) and composite symmetric zonal wind anomaly u'_s in D(0)JF(1) averaged over 1000–700 hPa for El Niño (shading; m s^{-1}).

antisymmetric meridional advection $-[v(\partial u/\partial y)]'_a$ is mainly determined by $-\overline{v}_a(\partial u'_s/\partial y)$ (Figs. 6a,b), that is, the advection of anomalous symmetric zonal wind by antisymmetric mean meridional wind.

Therefore, a mechanism for the southward wind shift is put forth based on the momentum budget diagnosis above. It involves a two-step process. The first step is the advection of the anomalous zonal wind by the climatological southward mean flow. Initially the zonal wind anomaly associated with ENSO is symmetric about the equator, and its maximum is right on the equator. This leads to a positive (negative) meridional gradient of the zonal wind anomaly south (north) of the equator. Because the winter mean flow has a pronounced southward component in the CEP (Fig. 6c), the mean wind advects the zonal wind anomaly southward. As a consequence, $-\overline{v}_a(\partial u'_s/\partial y)$ is positive in SH but negative in NH. Therefore, the advection of the zonal wind anomaly by the mean meridional flow is one of the major mechanisms for the southward wind shift.

What causes the southward climatological mean flow in the CEP in boreal winter? To address this question, we examine the mean precipitation and wind fields and their antisymmetric components in the tropical Pacific basin (Fig. 7). It is interesting to note that there is a great contrast in the cross-equatorial mean flow between the western and eastern parts of the basin (Fig. 7b). To the west, southward flows dominate, in association with heavier rainfall along the SPCZ. To the east, northward flows dominate, in association with greater precipitation along the intertropical convergence zone (ITCZ) north of the equator. The separation line between then lies at about 140°W. Therefore, the CEP is a region controlled by southward cross-equatorial mean flow in DJF.

b. *Pressure gradient and Coriolis force terms*

The antisymmetric zonal momentum budget analysis (Fig. 4g) indicates that beside the anomalous meridional advection, the positive zonal wind tendency south of the equator during El Niño arises from the antisymmetric pressure gradient force $-(\partial\varphi/\partial x)'_a$ and the Coriolis force fv'_a terms. To understand the relevant physical processes, we examine the horizontal pattern of the antisymmetric low-level wind, precipitation, and geopotential height anomaly fields (Figs. 8a,b). Note that there is a marked development of an antisymmetric mode in the CEP. This antisymmetric mode is characterized by a positive (negative) precipitation anomaly south (north) of the equator, a southward cross-equatorial wind anomaly, and a negative (positive) geopotential height anomaly center south (north) of the equator. On the one hand, a southward wind anomaly results in a positive zonal wind tendency in the SH due to the Coriolis force (Fig. 4d). On the other hand, a low pressure anomaly south of the equator near eastern boundary of the analysis domain leads to a positive zonal pressure gradient force (Fig. 4e). Thus, the development of the antisymmetric circulation and precipitation patterns holds a key for the positive contributions to the zonal wind tendency by the pressure gradient and Coriolis force terms.

Thus, the second step of the process involves the development of the antisymmetric mode. We argue that the following two positive feedback processes are responsible for the unstable development of the antisymmetric mode. The first positive feedback involves the moisture–convection–circulation feedback. The initial southward shift of the westerly anomaly is caused by the anomalous meridional advection $-\overline{v}(\partial u'/\partial y)$. Then the shifted westerly anomaly advects high mean moisture from the warm pool (Fig. 8e). This causes the increase of local moisture and moist static energy (MSE) (Fig. 8c), which further enhances the local precipitation in SH. The precipitation anomaly south of the equator drives an antisymmetric circulation response, which further strengthens the precipitation through the boundary layer convergence. Through this positive moisture–convection–circulation feedback, the antisymmetric mode grows.

The second positive feedback involves the wind–evaporation–SST (WES) feedback. The southward shift of the westerly during El Niño reduces the mean trade easterly wind in the region,

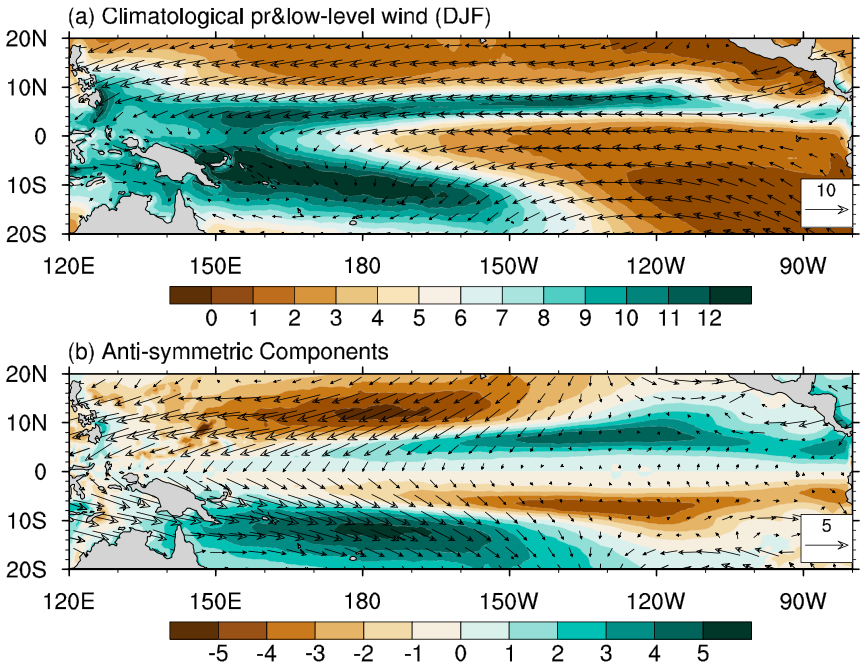

FIG. 7. (a) Horizontal patterns of climatological wind averaged over 1000–700 hPa (vector; $m\,s^{-1}$) and precipitation (shading; $mm\,day^{-1}$) in DJF. (b) As in (a), but for their antisymmetric components.

leading to the reduction of the surface wind speed and thus surface evaporation. This causes a warm SSTA south of the equator (Fig. 8d), which may further strengthen the cross-equatorial flow through a positive WES feedback process (e.g., Xie and Philander 1994; Li and Philander 1996; Li 1997b). Thus, the thermodynamic atmosphere–ocean interaction process also contributes to the development of an antisymmetric mode.

As a result of the two positive feedback processes, the initial shift due to the anomalous meridional advection is further amplified and extended farther to the south. The meridional–vertical structure of the antisymmetric mode can be represented by a pronounced anomalous vertical overturn circulation in the region (Fig. 8f).

To sum up, the zonal momentum budget analysis reveals two mechanisms responsible for the southward zonal wind shift. The first is the anomalous zonal wind advection by the climatological cross-equatorial wind. The second is the zonal wind acceleration caused by antisymmetric pressure gradient and Coriolis forces in the presence of a marked antisymmetric circulation/precipitation pattern in the CEP.

5. Sensitivity of atmospheric response to SSTA pattern and season

The composite SSTA pattern during the ENSO mature winter exhibits a slightly equatorial asymmetry, with a maximum SSTA center located at 1°S in the far eastern Pacific (Fig. 1; Su et al. 2010). Does this asymmetric SSTA play a role in the southward shift of the zonal wind anomaly in central Pacific? To address this question, we designed a set of sensitivity numerical experiments using an atmospheric general circulation model, ECHAM 4.6 (Roeckner et al. 1996). The model has a horizontal resolution of 2.8° × 2.8° (T42) and 19 vertical levels extending from the surface to 10 hPa.

A control experiment was first run with specified climatological monthly SST field. Then two sensitivity experiments were followed. In the first sensitivity experiment (EXP_SSTA), the model was forced by the climatological SST plus an anomalous SST pattern in DJF (Fig. 9a) derived from the El Niño composite. In the second sensitivity experiment (EXP_SSTA–sym), the model was forced by the climatological SST plus the symmetric component of the El Niño SSTA composite field (Fig. 9b). The SSTA pattern is added in all calendar months in the two sensitivity experiments. All these experiments were integrated for 20 years, and the outputs from the last 10 years were analyzed.

Figures 9c–f show the difference between the sensitivity experiments and the control experiment of the simulated precipitation and 850-hPa wind fields. The wind and precipitation responses in EXP_SSTA and EXP_SSTA–sym are remarkably similar (Figs. 9c,e). The zonal mean zonal wind anomaly in the CEP shows a clear southward shift (Figs. 9d,f), similar to the observation. The main difference between the two sensitivity experiments lies on the magnitude of the shifted zonal wind anomaly (Figs. 9d,f). The maximum westerly anomaly in EXP_SSTA reaches $8\,m\,s^{-1}$ while it is about $6\,m\,s^{-1}$ in EXP_SSTA–sym. This implies that antisymmetric SSTA can to a certain extent affects the zonal wind shift through the WES feedback, even though the effect of the moisture–convection–circulation feedback might be stronger.

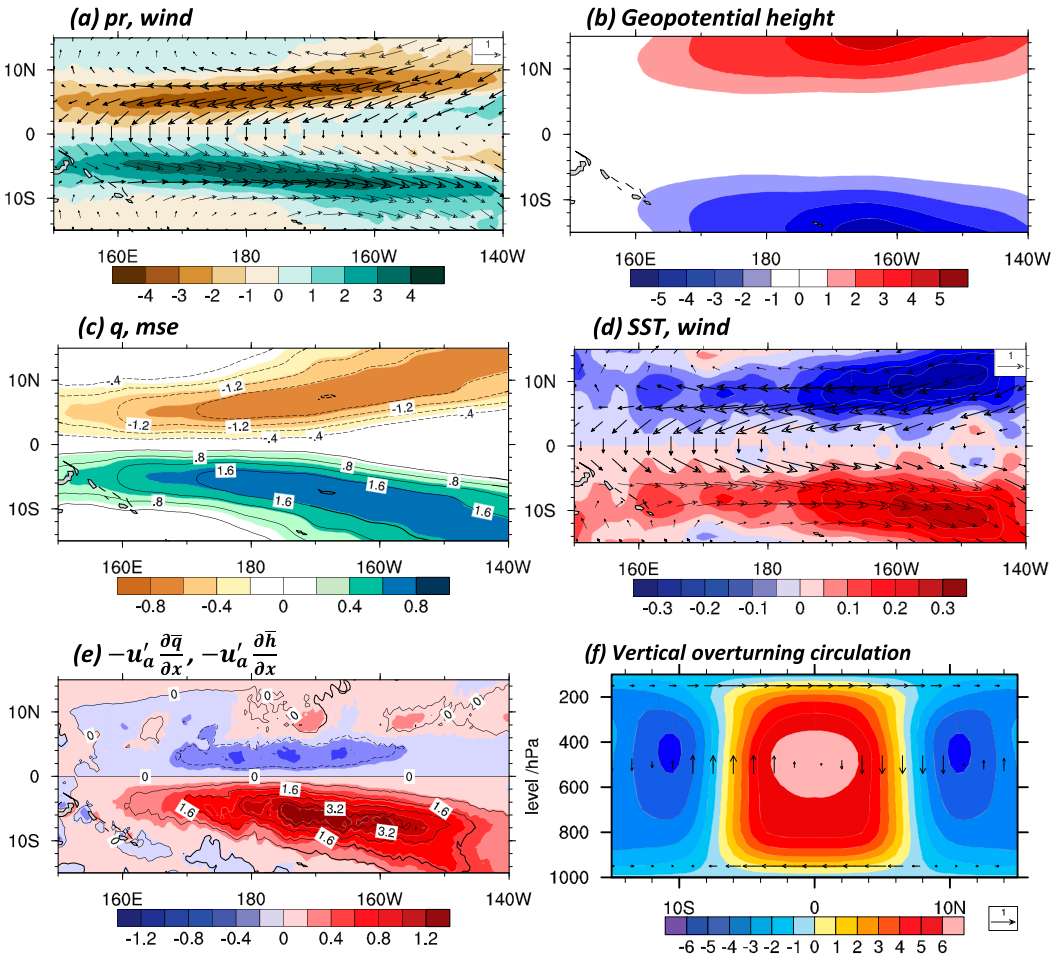

FIG. 8. Composite patterns of an antisymmetric mode during El Niño mature winter: (a) anomalous precipitation (shading; mm day^{-1}) and wind averaged over 1000–700 hPa (vector; m s^{-1}), (b) anomalous geopotential height field averaged over 1000–700 hPa (gpm), (c) anomalous specific humidity (shading; g kg^{-1}) and moist static energy (MSE) fields [contour interval: 0.4 × 10^3 W m^2; solid (dashed) line indicates positive (negative) value] averaged over 1000–700 hPa, where MSE = $C_pT + L_vq + \emptyset$, (d) anomalous SST (shading; K) and wind at 850 hPa (vector; m s^{-1}), (e) anomalous zonal moisture advection $-u'_a(\partial\bar{q}/\partial x)$ (shading; 10^9 s^{-1}) and moist enthalpy advection $-u'_a(\partial\bar{h}/\partial x)$ (contour; 10^3 W m^2 s^{-1}) averaged over 1000–700 hPa, where moist enthalpy $h = C_pT + L_vq$, and (f) anomalous streamfunction (10^6 m^2 s^{-1}) to represent a vertical overturning circulation averaged over 160°E–150°W. Arrows represent vertical velocity at 500 hPa and meridional velocity at 925 and 150 hPa.

A parallel diagnosis of the antisymmetric zonal momentum budget is conducted for the AGCM simulation. Figure 10 shows the horizontal distribution of each of the antisymmetric zonal momentum budget terms in EXP_SSTA–sym. The green box denotes the region of the maximum anomalous westerly wind and the maximum anomalous westerly tendency simulated by the AGCM. Figure 11a illustrates the box-averaged values of the budget terms. The two leading positive tendency terms are 1) the meridional advection term and 2) the pressure gradient force term. This is consistent with that from the observational diagnosis. The main difference between the observation and simulation lies on the Coriolis force term. It is speculated that the difference is attributed to the model bias in zonal location of the simulated zonal wind anomaly. The budget terms in EXP_SSTA in general resemble those in EXP_SSTA–sym (Fig. 11b).

In contrast to boreal winter, the SPCZ in boreal summer becomes weaker and withdraws westward. Maximum precipitation appears along the ITCZ north of the equator, and there is pronounced northward cross-equatorial flow in the western and central Pacific. It is anticipated that such a mean state change could affect the anomalous atmospheric response.

To demonstrate the mean state effect, we conducted another set of two sensitivity experiments in which the model was forced by the same SSTA patterns as in the previous sensitivity experiments but under the boreal summer (JJA) background mean condition. Figure 10 shows the simulated precipitation and wind responses. Note that the maximum zonal wind anomaly

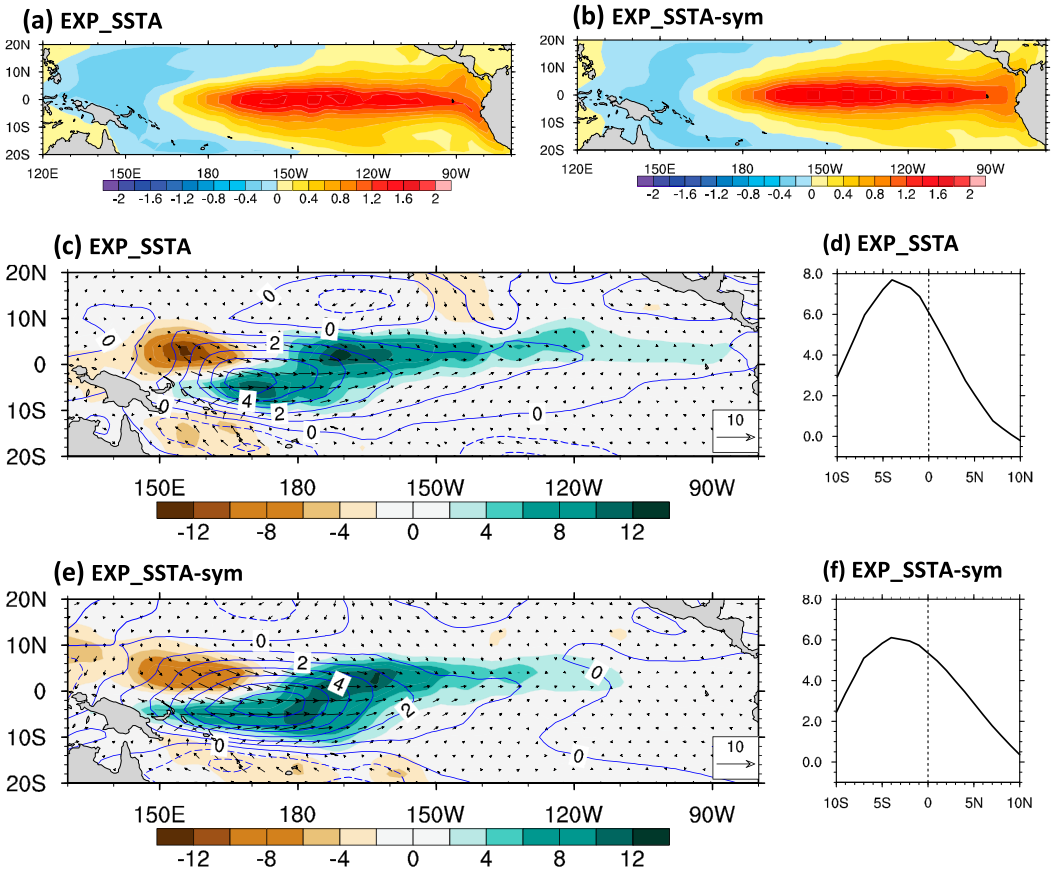

FIG. 9. (a),(b) The SSTA patterns specified in EXP_SSTA and EXP_SSTA–sym. (c),(e) Anomalous 850-hPa wind (wind: vector; u: contour; m s^{-1}) and precipitation (shading; mm day^{-1}) responses in DJF to the specified SSTA forcing in EXP_SSTA and (d) EXP_SSTA–sym. (d),(f) Meridional profiles of the simulated zonal wind anomaly averaged over 150°E–170°W.

now shifts northward in both the experiments (Figs. 12a,c). Such a northward shift is also seen in the zonal mean zonal wind fields (Figs. 12b,d). However, the northward shift in boreal summer is weaker than the southward shift in boreal winter, which is primarily attributed to the larger background mean cross-equatorial wind in boreal winter. Thus, the numerical model experiments clearly demonstrate the importance of the seasonal mean state in determining the meridional shift the zonal wind anomaly associated with ENSO.

6. Summary and discussion

A composite analysis of the ERA reanalysis dataset revealed a marked equatorial asymmetry of low-level zonal wind anomalies in CEP during the ENSO mature winters. The maximum westerly (easterly) anomaly center during El Niño (La Niña) shifted from the equator in the preceding season to a southern location in boreal winter. The zonal wind anomaly center reached the southernmost position in February and then weakened as it gradually moved back to the equator.

An antisymmetric zonal momentum budget diagnosis was performed to understand the mechanisms responsible for generating the equatorially asymmetric zonal wind tendency between SH and NH in boreal winter. The result indicates that the antisymmetric zonal wind tendency was attributed to the advection of the symmetric zonal wind anomaly by antisymmetric meridional mean flow and antisymmetric zonal pressure gradient and Coriolis forces, the latter of which was closely associated with the development of an unstable antisymmetric mode in CEP.

Figure 13 is a schematic diagram illustrating the two-step process for the southward shift of the westerly anomaly during El Niño. The first step involves the advection of the anomalous zonal wind by the climatological southward cross-equatorial wind. As the sun moves to the SH in boreal winter, the rainfall along the SPCZ strengthens, leading to a southward cross-equatorial mean flow. This antisymmetric mean flow advects the El Niño westerly into the SH.

The second step involves the amplification and farther southward extension of the zonal wind anomaly, which are accompanied by the development of an antisymmetric mode in the CEP (Fig. 8). Two positive feedbacks are responsible for the growth of the antisymmetric mode. The first positive feedback involves a moisture–convection–circulation feedback. The initial shift of the

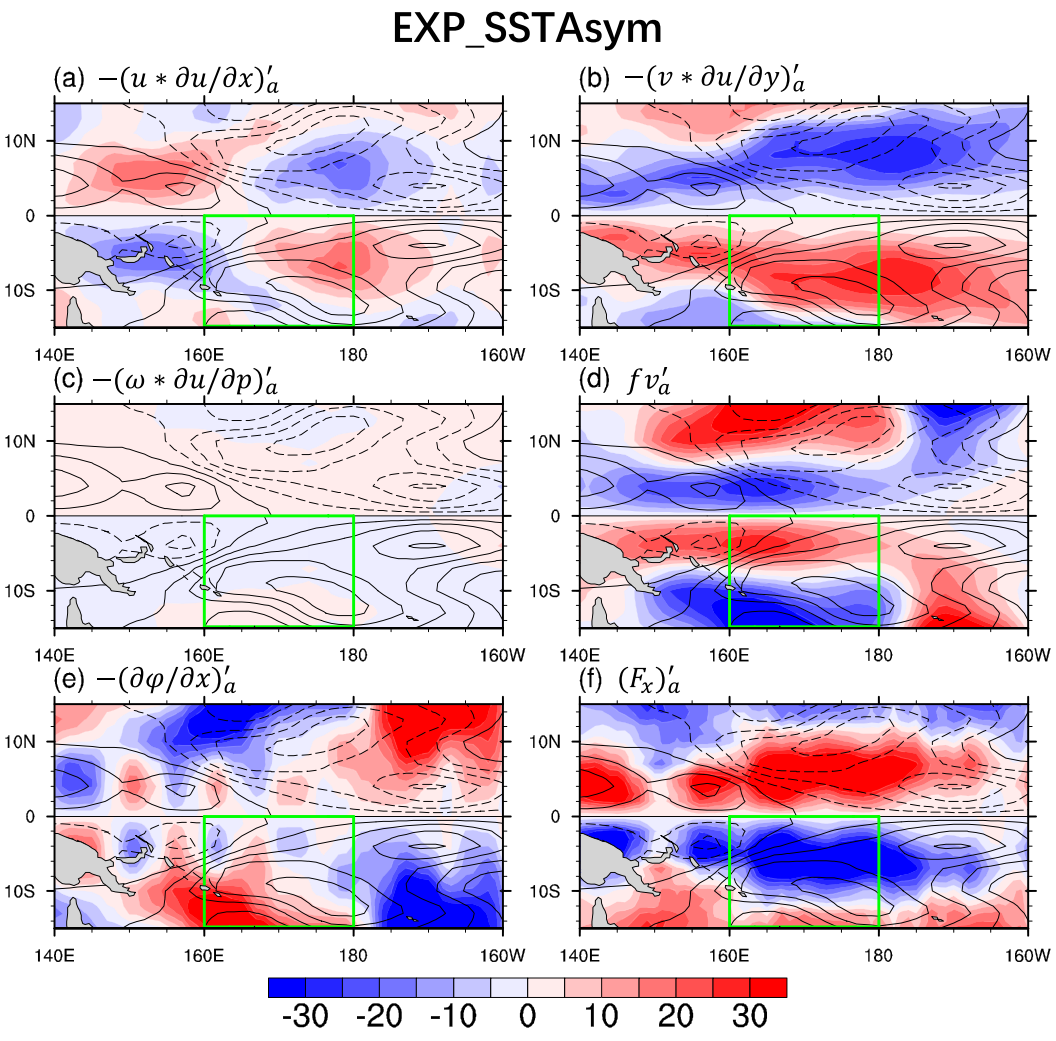

FIG. 10. The patterns of the composite antisymmetric zonal momentum budget terms in DJF for EXP_SSTAsym (shading) in (a) $-[u(\partial u/\partial x)]'_a$, (b) $-[v(\partial u/\partial y)]'_a$, (c) $-[\omega(\partial u/\partial p)]'_a$, (d) fv'_a, (e) $-(\partial\varphi/\partial x)'_a$, (f) $(F_x)'_a$ ($\mathrm{m\,s^{-1}\,month^{-1}}$). Contours in (a)–(f) represent the antisymmetric anomalous zonal wind tendency $(\partial u/\partial t)'_a$ (interval: 0.1 $\mathrm{m\,s^{-1}\,month^{-1}}$). The green box (160°E–180°, 0°–15°S) denotes the region of the maximum anomalous westerly wind and the maximum anomalous westerly tendency.

westerly by the anomalous meridional advection causes a positive moisture advection anomaly south of the equator as the mean moisture is higher in the western Pacific warm pool. This leads to the increase of moisture and moist enthalpy (or MSE) south of the equator. The increased low-level moisture and moist enthalpy promote a positive precipitation anomaly in situ, leading to the development of antisymmetric circulation. The so generated cross-equatorial wind anomaly may further strengthen the precipitation anomaly through enhanced boundary layer convergence. Through this positive moisture–convection–circulation feedback, the antisymmetric mode develops.

The second positive feedback involves the atmosphere–ocean interaction. It was found that an antisymmetric SSTA pattern, with a warm (cold) anomaly south (north) of the equator, also develops during El Niño mature winter. The antisymmetric SSTA pattern results from reduced wind speed and surface evaporation south of the equator, because the shifted westerly anomaly tends to offset the mean trade easterly. The antisymmetric SSTA pattern further strengthens the anomalous cross-equatorial flow. Through the positive wind–evaporation–SST feedback the antisymmetric SSTA pattern develops.

As a consequence of the two positive feedbacks, the antisymmetric mode develops in CEP during El Niño mature winter. This mode is characterized by a southward cross-equatorial wind and a low pressure center south of the equator, which contribute a positive westerly tendency south of the equator through the combined pressure gradient and Coriolis forces.

Idealized numerical model experiments were carried out to understand the role of the anomalous SSTA patterns and the

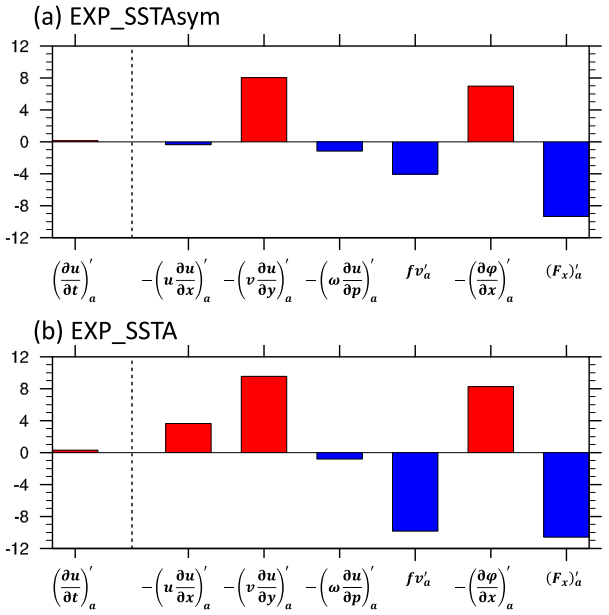

FIG. 11. (a) The individual budget terms ($\mathrm{m\,s^{-1}\ month^{-1}}$) averaged over the green box shown in Fig. 10 for EXP_SSTA–sym. (b) As in (a), but for EXP_SSTA.

mean flow in causing the southward wind shift. The results show that a perfectly symmetric SSTA pattern is able to simulate the same westerly southward shift during El Niño mature winter, suggesting that the shift is primarily attributed to moisture–convection–circulation feedback in CEP, while the effect of WES feedback is relatively weaker. The boreal winter background mean state is critical to cause the southward shift. Given the same SSTA pattern, the zonal wind anomaly shifts to the SH during boreal winter but to the NH during boreal summer.

An open question is why the unstable development of the antisymmetric mode happened in the CEP. It is argued that the following two factors are critical. The first is the zonal location of the maximum zonal wind anomaly. It is typical that in response to ENSO SSTA forcing, a maximum zonal wind anomaly center is located in the CEP. The second is the zonal location of the maximum cross-equatorial wind (Fig. 6c). It is the combination of the two factors that determines the favorable location for the southward shift.

The current result differs from McGregor et al. (2012), who suggested that a weaker boundary layer damping coefficient favored a stronger westerly tendency south of the equator. Our momentum budget diagnosis shows that the friction term always offsets the zonal wind tendency and the damping effect is greater south of the equator. It is worth mentioning that the term F_x in the current analysis was calculated based on the residual of the momentum budget. Therefore, it represents surface friction as well as unresolved subgrid processes such as turbulent viscosity, diffusion, and subgrid vertical mixing. In the current study we focused on investigating the mechanism responsible for the southward shift of anomalous westerly (easterly) during El Niño (La Niña). Given that El Niño exhibits different flavors in its spatial pattern (i.e., EP-type and CP-type), would the two types of El Niño behave differently in terms of their zonal wind shift characteristics and mechanism? We will address this question in near future in lieu of ENSO pattern diversity.

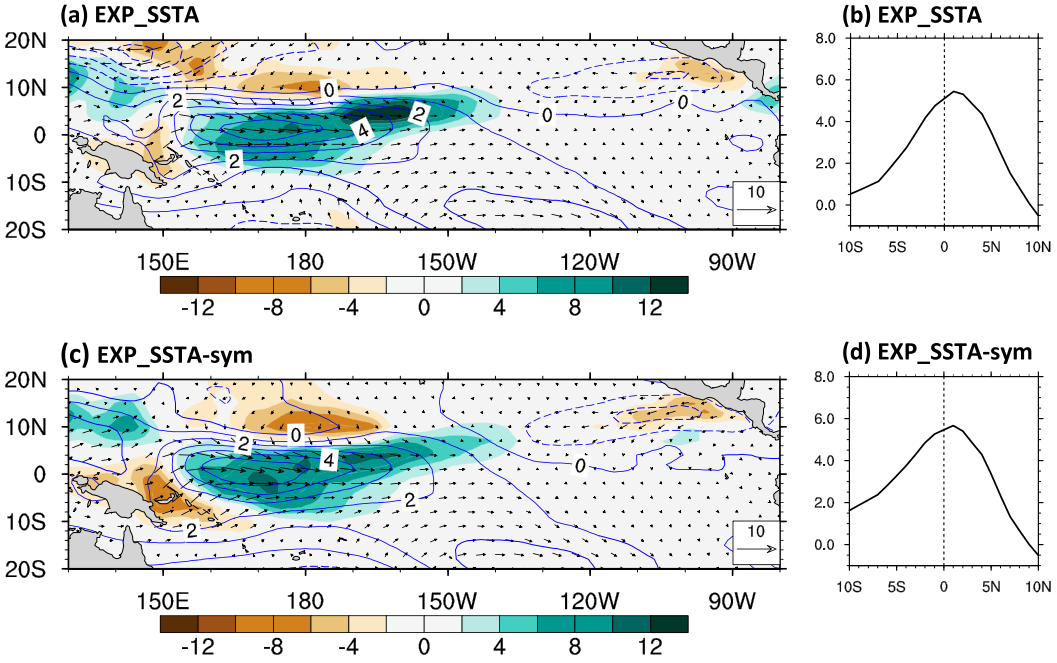

FIG. 12. As in Figs. 9c–f, but for the boreal summer season (JJA).

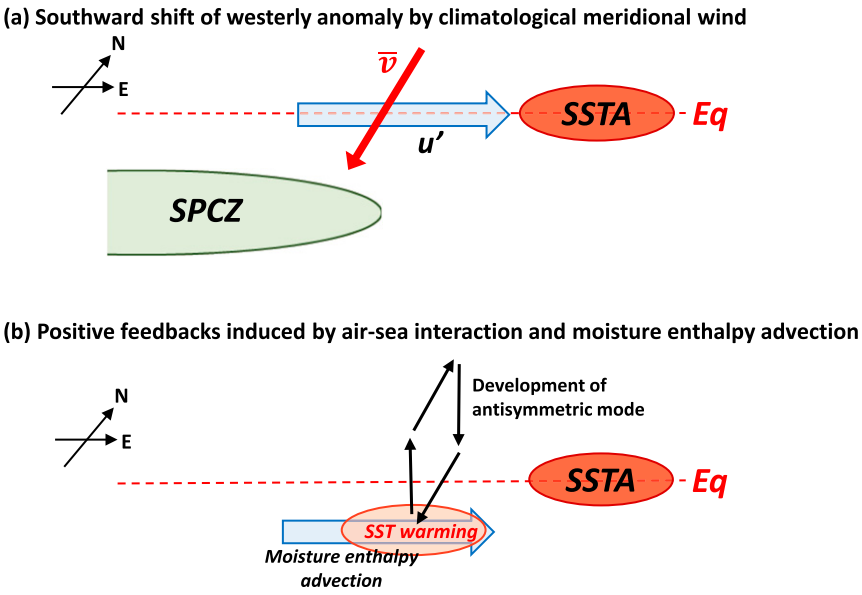

FIG. 13. Schematic diagrams illustrating the two-step process responsible for the southward shift of the westerly anomaly during El Niño: (a) the advection of the anomalous westerly by the climatological mean southward cross-equatorial flow and (b) the development of an antisymmetric mode through a positive moisture–convection–circulation feedback triggered by anomalous moisture enthalpy advection and a positive wind–evaporation–SST feedback triggered by reduced wind speed.

Acknowledgments. This work was supported by NSFC Grants 42088101 and 41630423, NSF AGS-2006553, and NOAA NA18OAR4310282. This is SOEST contribution number 11410, IPRC contribution number 1538, and ESMC contribution 355.

Data availability statement. The HadISST dataset is from the Met Office Hadley Centre (http://www.metoffice.gov.uk/hadobs/). ERA-Interim data were downloaded from the European Centre for Medium-Range Weather Forecasts (ECMWF) (http://www.ecmwf.int/en/research/climate-reanalysis/era-interim).

REFERENCES

Abellán, E., and S. McGregor, 2016: The role of the southward wind shift in both the seasonal synchronization and duration of ENSO events. *Climate Dyn.*, **47**, 509–527, https://doi.org/10.1007/s00382-015-2853-1.

——, ——, and M. H. England, 2017: Analysis of the southward wind shift of ENSO in CMIP5 models. *J. Climate*, **30**, 2415–2435, https://doi.org/10.1175/JCLI-D-16-0326.1.

An, S.-I., and B. Wang, 2001: Mechanisms of locking of the El Niño and La Niña mature phases to boreal winter. *J. Climate*, **14**, 2164–2176, https://doi.org/10.1175/1520-0442(2001)014<2164:MOLOTE>2.0.CO;2.

Bayr, T., D. Dommenget, T. Martin, and S. B. Power, 2014: The eastward shift of the Walker circulation in response to global warming and its relationship to ENSO variability. *Climate Dyn.*, **43**, 2747–2763, https://doi.org/10.1007/s00382-014-2091-y.

——, M. Latif, D. Dommenget, C. Wengel, J. Harlaß, and W. Park, 2018: Mean-state dependence of ENSO atmospheric feedbacks in climate models. *Climate Dyn.*, **50**, 3171–3194, https://doi.org/10.1007/s00382-017-3799-2.

——, A. Drews, M. Latif, and J. Lübbecke, 2021: The interplay of thermodynamics and ocean dynamics during ENSO growth phase. *Climate Dyn.*, **56**, 1681–1697, https://doi.org/10.1007/s00382-020-05552-4.

Cane, M. A., and S. E. Zebiak, 1985: A theory for El Niño and the Southern Oscillation. *Science*, **228**, 1085–1087, https://doi.org/10.1126/science.228.4703.1085.

Chen, M., T. Li, X. Shen, and B. Wu, 2016: Relative roles of dynamic and thermodynamic processes in causing evolution asymmetry between El Niño and La Niña. *J. Climate*, **29**, 2201–2220, https://doi.org/10.1175/JCLI-D-15-0547.1.

Dee, D. P., and S. Uppala, 2009: Variational bias correction of satellite radiance data in the ERA-Interim reanalysis. *Quart. J. Roy. Meteor. Soc.*, **135**, 1830–1841, https://doi.org/10.1002/qj.493.

Dommenget, D., and Y. Yu, 2016: The seasonally changing cloud feedbacks contribution to the ENSO seasonal phase-locking. *Climate Dyn.*, **47**, 3661–3672, https://doi.org/10.1007/s00382-016-3034-6.

Gadgil, S., P. Joseph, and N. Joshi, 1984: Ocean–atmosphere coupling over monsoon regions. *Nature*, **312**, 141–143, https://doi.org/10.1038/312141a0.

Graham, N., and T. Barnett, 1987: Sea surface temperature, surface wind divergence, and convection over tropical oceans. *Science*, **238**, 657–659, https://doi.org/10.1126/science.238.4827.657.

Harrison, D. E., 1987: Monthly mean island surface winds in the central tropical Pacific and El Niño events. *Mon. Wea. Rev.*, **115**, 3133–3145, https://doi.org/10.1175/1520-0493(1987)115<3133:MMISWI>2.0.CO;2.

——, and G. A. Vecchi, 1999: On the termination of El Niño. *Geophys. Res. Lett.*, **26**, 1593–1596, https://doi.org/10.1029/1999GL900316.

Kang, I.-S., and J.-S. Kug, 2002: El Niño and La Niña sea surface temperature anomalies: Asymmetry characteristics associated with their wind stress anomalies. *J. Geophys. Res.*, **107**, 4372, https://doi.org/10.1029/2001JD000393.

Lengaigne, M., and G. A. Vecchi, 2010: Contrasting the termination of moderate and extreme El Niño events in coupled general circulation models. *Climate Dyn.*, **35**, 299–313, https://doi.org/10.1007/s00382-009-0562-3.

——, J.-P. Boulanger, C. Menkes, and H. Spencer, 2006: Influence of the seasonal cycle on the termination of El Niño events in a coupled general circulation model. *J. Climate*, **19**, 1850–1868, https://doi.org/10.1175/JCLI3706.1.

Li, T., 1997a: Phase transition of the El Niño–Southern Oscillation: A stationary SST mode. *J. Atmos. Sci.*, **54**, 2872–2887, https://doi.org/10.1175/1520-0469(1997)054<2872:PTOTEN>2.0.CO;2.

——, 1997b: Air–sea interactions of relevance to the ITCZ: Analysis of coupled instabilities and experiments in a hybrid coupled GCM. *J. Atmos. Sci.*, **54**, 134–147, https://doi.org/10.1175/1520-0469(1997)054<0134:ASIORT>2.0.CO;2.

——, and S. G. H. Philander, 1996: On the annual cycle of the eastern equatorial Pacific. *J. Climate*, **9**, 2986–2998, https://doi.org/10.1175/1520-0442(1996)009<2986:OTACOT>2.0.CO;2.

——, and P.-C. Hsu, 2018: Dynamics of El Niño–Southern Oscillation. *Fundamentals of Tropical Climate Dynamics*. Springer, 149–183.

——, B. Wang, and L. Wang, 2016: Comments on ''Combination mode dynamics of the anomalous northwest Pacific anticyclone.'' *J. Climate*, **29**, 4685–4693, https://doi.org/10.1175/JCLI-D-15-0385.1.

McGregor, S., A. Timmermann, N. Schneider, M. F. Stuecker, and M. H. England, 2012: The effect of the South Pacific convergence zone on the termination of El Niño events and the meridional asymmetry of ENSO. *J. Climate*, **25**, 5566–5586, https://doi.org/10.1175/JCLI-D-11-00332.1.

——, N. Ramesh, P. Spence, M. H. England, M. J. McPhaden, and A. Santoso, 2013: Meridional movement of wind anomalies during ENSO events and their role in event termination. *Geophys. Res. Lett.*, **40**, 749–754, https://doi.org/10.1002/grl.50136.

Philander, S. G., 1990: *El Niño, La Niña, and the Southern Oscillation*. International Geophysics Series, Vol. 46, Academic Press, 293 pp.

Rasmusson, E. M., and T. H. Carpenter, 1982: Variations in tropical sea surface temperature and surface wind fields associated with the Southern Oscillation/El Niño. *Mon. Wea. Rev.*, **110**, 354–384, https://doi.org/10.1175/1520-0493(1982)110<0354:VITSST>2.0.CO;2.

Rayner, N., D. E. Parker, E. B. Horton, C. K. Folland, L. V. Alexander, D. P. Rowell, E. C. Kent, and A. Kaplan, 2003: Global analyses of sea surface temperature, sea ice, and night marine air temperature since the late nineteenth century. *J. Geophys. Res.*, **108**, 4407, https://doi.org/10.1029/2002JD002670.

Roeckner, E., and Coauthors, 1996: The atmospheric general circulation model ECHAM-4: Model description and simulation of present-day climate. Max-Planck-Institute for Meteorology Rep. 218, 90 pp., http://www.mpimet.mpg.de/fileadmin/publikationen/Reports/MPI-Report_218.pdf.

Ropelewski, C. F., and M. S. Halpert, 1987: Global and regional scale precipitation patterns associated with the El Niño/Southern Oscillation. *Mon. Wea. Rev.*, **115**, 1606–1626, https://doi.org/10.1175/1520-0493(1987)115<1606:GARSPP>2.0.CO;2.

Spencer, H., 2004: Role of the atmosphere in seasonal phase locking of El Niño. *Geophys. Res. Lett.*, **31**, L24104, https://doi.org/10.1029/2004GL021619.

Stein, K., N. Schneider, A. Timmermann, and F.-F. Jin, 2010: Seasonal synchronization of ENSO events in a linear stochastic model. *J. Climate*, **23**, 5629–5643, https://doi.org/10.1175/2010JCLI3292.1.

Stuecker, M. F., A. Timmermann, F.-F. Jin, S. McGregor, and H.-L. Ren, 2013: A combination mode of the annual cycle and the El Niño/Southern Oscillation. *Nat. Geosci.*, **6**, 540–544, https://doi.org/10.1038/ngeo1826.

——, F.-F. Jin, A. Timmermann, and S. McGregor, 2015: Combination mode dynamics of the anomalous northwest Pacific anticyclone. *J. Climate*, **28**, 1093–1111, https://doi.org/10.1175/JCLI-D-14-00225.1.

Su, J., R. Zhang, T. Li, X. Rong, J.-S. Kug, and C.-C. Hong, 2010: Causes of the El Niño and La Niña amplitude asymmetry in the equatorial eastern Pacific. *J. Climate*, **23**, 605–617, https://doi.org/10.1175/2009JCLI2894.1.

Taschetto, A. S., C. C. Ummenhofer, M. F. Stuecker, D. Dommenget, K. Ashok, R. R. Rodrigues, and S.-W. Yeh, 2020: ENSO atmospheric teleconnections. *El Niño Southern Oscillation in a Changing Climate, Geophys. Monogr.*, Vol. 253, Amer. Geophys. Union, 309–335.

Trenberth, K. E., and J. M. Caron, 2000: The Southern Oscillation revisited: Sea level pressures, surface temperatures, and precipitation. *J. Climate*, **13**, 4358–4365, https://doi.org/10.1175/1520-0442(2000)013<4358:TSORSL>2.0.CO;2.

Vecchi, G. A., 2006: The termination of the 1997–98 El Niño. Part II: Mechanisms of atmospheric change. *J. Climate*, **19**, 2647–2664, https://doi.org/10.1175/JCLI3780.1.

——, and D. E. Harrison, 2003: On the termination of the 2002–03 El Niño event. *Geophys. Res. Lett.*, **30**, 1964, https://doi.org/10.1029/2003GL017564.

Wallace, J., E. Rasmusson, T. Mitchell, V. Kousky, E. Sarachik, and H. von Storch, 1998: On the structure and evolution of ENSO-related climate variability in the tropical Pacific: Lessons from TOGA. *J. Geophys. Res. Oceans*, **103**, 14 241–14 259, https://doi.org/10.1029/97JC02905.

Wang, B., R. Wu, and X. Fu, 2000: Pacific–East Asian teleconnection: How does ENSO affect East Asian climate? *J. Climate*, **13**, 1517–1536, https://doi.org/10.1175/1520-0442(2000)013<1517:PEATHD>2.0.CO;2.

Wengel, C., M. Latif, W. Park, J. Harlaß, and T. Bayr, 2018: Seasonal ENSO phase locking in the Kiel Climate Model: The importance of the equatorial cold sea surface temperature bias. *Climate Dyn.*, **50**, 901–919, https://doi.org/10.1007/s00382-017-3648-3.

Xie, S.-P., and S. G. H. Philander, 1994: A coupled ocean–atmosphere model of relevance to the ITCZ in the eastern Pacific. *Tellus*, **46A**, 340–350, https://doi.org/10.3402/tellusa.v46i4.15484.

Yanai, M., S. Esbensen, and J.-H. Chu, 1973: Determination of bulk properties of tropical cloud clusters from large-scale heat and moisture budgets. *J. Atmos. Sci.*, **30**, 611–627, https://doi.org/10.1175/1520-0469(1973)030<0611:DOBPOT>2.0.CO;2.